

The Role of Carbon Electrodes Pore Size Distribution on the Formation of the Cathode–Electrolyte Interphase in Lithium–Sulfur Batteries

Christian Kensy,^[a, b] Desirée Leistenschneider,^[c] Shuwen Wang,^[d] Hideki Tanaka,^[d] Susanne Dörfler,^[b] Katsumi Kaneko,^[d] and Stefan Kaskel^{*[a, b]}

The use of sulfur is advantageous in next generation lithium batteries replacing scarce metals and leading to enhanced specific energy compared to established energy storage devices. Herein, the utilization of microporous ($d < 2 \text{ nm}$) carbon/sulfur composites using a carbonate-based electrolyte is studied to obtain more insights into the formation of a solid-electrolyte interphase (SEI) layer on the cathode surface (cathode-electrolyte interphase, CEI) in Li-S cells. The sulfur was confined in model carbide-derived carbon (CDC) system with uniform micropores as well as in commercial microporous activated carbon materials. The molecular structure of sulfur in

the pores is characterized by means of EXAFS spectroscopy. The electrochemical evaluation of confined sulfur cathodes revealed quasi solid-state transformation mechanism as well as the generation of a protective SEI layer on the cathode surface. This cathode-electrolyte interphase (CEI) allows common microporous carbon/sulfur cathodes to reversibly cycle in carbonate-based electrolyte, while mesoporous systems show rapid capacity fade due to permeable CEIs. Based on this result, the influence of the porosity of the porous carbon host materials on the essential cathodic SEI layer formation is discussed for carbonate-based electrolytes in Li-S batteries.

1. Introduction

Lithium-sulfur (Li-S) batteries have attracted enormous attention over the past decades to overcome limitations regarding specific energy of common established lithium-ion batteries (LiB).^[1] The promising properties of sulfur, e.g. high theoretical capacity (1672 mAh g_s⁻¹) or high theoretical energy density (2500 Wh kg⁻¹), coupled with a Li metal anode (3860 mAh g_s⁻¹) enable a low-cost, non-toxic and lightweight alternative for applications in drones, high altitude pseudosatellites and aerospace technology.^[2,3] Although there are numerous promising features of sulfur as cathode active material, a few inherent technological challenges still hinder a widespread commercial-

ization of Li-S cells. An important aspect is the stabilization of the metallic lithium anode and minimization of lithium excess and corrosion. In addition, polysulfide (PS) shuttling for current standard ether-based electrolyte system (1 M LiTFSI in DME/DOL (v:v=1:1)) and hence, capacity fading due to active material loss have to be overcome.^[4] To address these issues, a variety of strategies, in particular the development of new electrolytes^[5], metal additives^[6] or novel polar cathode materials^[7], have been investigated. However, by using standard DME/DOL electrolyte with commercially available carbonaceous scaffold materials, e.g. Ketjenblack, the theoretical capacity of sulfur has not yet been fully exploited and it appears the solid-liquid-solid conversion mechanism reaches an upper limit.^[8-10]

In order to utilize a higher mass fraction of active material, a particular approach is to confine sulfur into pores or bind it to special polymers and use carbonate-based electrolytes.^[11-28] In this system, the confinement is required as polysulfides would otherwise attack the carbonates.^[29] The voltage profiles differ from those of commonly analyzed Li-S batteries with standard ether-based electrolyte, where two discharge plateaus at 2.40 V and 2.10 V are normally observed according to the formation of high-order PS (Li₂S₆₋₈) and transformation of short-chain PS (Li₂S₂₋₄) to Li₂S, respectively.^[8,30] Confined sulfur cathodes instead show only one discharge plateau at 1.70 V.^[11-28] Surprisingly, the voltage profiles of the liquid carbonate-based electrolytes are comparable to those of all-solid state Li-S cells^[31,32] and of sulfurized^[33] or selenium-doped^[34] polyacrylonitrile (PAN) cathodes with covalently bound sulfur, respectively. Various concepts have been discussed for the single discharge plateau phenomenon. Wang *et al.* proposed a quasi-solid-state conversion mechanism which

[a] C. Kensy, Prof. Dr. S. Kaskel
Department of Inorganic Chemistry I
Technische Universität Dresden
Bergstraße 66, 01069 Dresden, Germany
E-mail: stefan.kaskel@tu-dresden.de

[b] C. Kensy, Dr. S. Dörfler, Prof. Dr. S. Kaskel
Department of Surface and Battery Technology
Fraunhofer Institute of Material and Beam Technology (IWS)
Winterbergstraße 28, 01277 Dresden, Germany

[c] Dr. D. Leistenschneider
Department of Chemical and Materials Engineering (CME)
University of Alberta
116 St. and 85 Ave, Edmonton, Canada AB T6G 2R3

[d] Dr. S. Wang, Prof. Dr. H. Tanaka, Prof. Dr. K. Kaneko
Department of Research Initiative for Supra-Materials (RISM)
Shinshu University
4-17-1 Wakasato, Nagano-City, Japan

 Supporting information for this article is available on the WWW under
<https://doi.org/10.1002/batt.202000195>

 © 2020 The Authors. *Batteries & Supercaps* published by Wiley-VCH GmbH.
This is an open access article under the terms of the Creative Commons Attribution License, which permits use, distribution and reproduction in any medium, provided the original work is properly cited.

results from the reaction of desolvated Li^+ ions with confined sulfur in micropores under solvent deficient conditions. According to the desolvation effect, the dissolution of PS intermediates is hindered and hence, the sulfur is utilized via quasi-solid-state reactions.^[31,35] Moreover, DFT calculations illustrated that only short-chain sulfur forms (S_{2-4}) can be hosted in ultramicropores (pore width $< 0.70 \text{ nm}$) since their chain-like structures have at least one dimension below 0.50 nm.^[12,24] Therefore, for these studies the formation of long-chain PS is suppressed due to the trapping properties of the over-lapping interaction potentials of neighboring pore walls inside the carbonaceous host. However, the real bonding nature of the sulfur inside those micro- or ultramicropores has not been yet fully uncovered. Additionally, it is known that the quasi-solid-state conversion is realized due to the formation of a solid-electrolyte interphase (SEI) on the cathode surface during the initial discharge process.^[13,16,21,36] Thus, a protective SEI layer is generated as a result of the nucleophilic reaction of PS intermediates with carbonate molecules of the electrolyte or decomposition processes at the carbon surface.^[16,27,29] Based on these findings it was reasoned that the confinement of the small sulfur species is not necessary for enabling a quasi-solid-state conversion mechanism.^[21,24,36]

In the following, we propose a microporous carbide-derived-carbon (CDC) material as model scaffold to introduce confined sulfur into the micropores. CDC materials are obtained by halogenation of ceramic carbides.^[37] By the removal of metal or silicon atoms as halides the carbon backbone remains and a uniform pore size distribution is obtained exhibiting high specific surface areas and tunable pore sizes with narrow distributions. This class of carbon enables excellent performances in supercapacitors or as carbon scaffolds in Li-S batteries.^[37-39] The use of TiC-CDC with a uniform micropore (pore width $\sim 0.72 \text{ nm}$) allows the fundamental investigation of the sulfur adsorption process in micropores. The confinement of sulfur is realized by using a melt-infiltration at 155 °C followed by an evaporation process at 300 °C to remove excess sulfur.^[17,20,22] The sulfur confinement is successfully transferred to commercially available microporous activated carbon materials. Hence, the porosity changes of the C/S composites are characterized to show that sulfur is trapped inside the pores. We use X-ray absorption spectroscopy (XAS) as well as extended X-ray absorption fine-structure (EXAFS) to analyze the nature of the adsorbed sulfur molecules and achieve a better understanding of the atomic distribution of confined sulfur species, respectively. By evaluating the confined sulfur cathodes with carbonate-based LP30 electrolyte, we study their ability to utilize confined sulfur via quasi-solid-state conversion mechanism. Consequently, the SEI formation during the initial discharge is investigated. Based on these findings, the importance of carbon porosity on the SEI generation is discussed.

2. Results and Discussion

The synthesis of carbon/sulfur (C/S) composites with confined sulfur was realized by a melt-infiltration process followed by an evaporation procedure. The carbon materials were mixed with pristine sulfur in a defined weight ratio (2:3 or 1:1) and melt-infiltrated at 155 °C for 12 h (labeled as carbon-S). After melt-infiltration, excess sulfur was evaporated at 300 °C for 2 h under argon atmosphere (labeled as carbon-S_300) as reported elsewhere.^[17,20,22] This synthesis route was equally applicable to various commercially available microporous carbons.

2.1. Material Characterization

All carbon materials were investigated by nitrogen physisorption at -196 °C (Figure 1). The pristine carbons exhibit a type I(b) isotherm according to the IUPAC classification^[40], and high specific surface areas (SSA) of $1664 \text{ m}^2 \text{ g}^{-1}$ (TiC-CDC), $1653 \text{ m}^2 \text{ g}^{-1}$ (Cabot) and $1523 \text{ m}^2 \text{ g}^{-1}$ (YP), respectively. According to the pore size distribution (PSD) (Figure 1(b)), one maximum at 0.72 nm and a small peak at 1.19 nm are determined for TiC-CDC. In contrast, the commercial materials show a significant peak at 0.79 nm and, especially Cabot, a wider distribution for the second maxima ($\sim 1.19 \text{ nm}$) (Figure 1(e)). Hence, all microporous carbons contain predominantly supermicropores (0.70–2.00 nm) and a small percentage of ultramicropores ($< 0.70 \text{ nm}$).^[40]

In addition, the pristine carbon materials were characterized by Raman spectroscopy and SEM analysis to compare particle morphology and the degree of graphitization. Raman spectra (Figure S3) display the two significant bands for carbon materials at $\sim 1345 \text{ cm}^{-1}$ (D-band) and $\sim 1595 \text{ cm}^{-1}$ (G-band). The G-band correlates to the symmetrical stretching mode of graphitic domains with sp^2 hybridization, while D-band arises from the breathing mode in the presence of disorder or defects.^[41] The degree of graphitization I_D/I_G is calculated using a Lorentzian function. This ratio can point to differences in graphitization degrees of carbon materials and the length of graphene like structures inside the carbon backbone.^[39] The carbon samples TiC-CDC and YP exhibit comparable I_D/I_G ratios of 1.00. In contrast, Cabot shows a slightly higher I_D/I_G value of 1.10, which could possibly indicate more disordered structures and a higher amount of defects. According to the SEM images (Figure S4) YP and TiC-CDC reveal similar particle sizes and morphologies, whereas the Cabot material exhibits a wide particle size distribution.

Subsequently, all carbon scaffolds were infiltrated with elemental sulfur. Since the pores are filled with sulfur after infiltration process, drastically decreased SSAs for TiC-CDC-S ($79 \text{ m}^2 \text{ g}^{-1}$), Cabot-S ($35 \text{ m}^2 \text{ g}^{-1}$) and YP-S ($15 \text{ m}^2 \text{ g}^{-1}$) are observed (Table 1). Additionally, the total pore volumes as well as the micro pore volumes of the melt-infiltrated samples significantly drop (Table 1). However, after the evaporation process, the values of SSA and total pore volume of TiC-CDC-S_300 ($462 \text{ m}^2 \text{ g}^{-1}$, $0.30 \text{ cm}^3 \text{ g}^{-1}$), Cabot-S_300 ($295 \text{ m}^2 \text{ g}^{-1}$, $0.18 \text{ cm}^3 \text{ g}^{-1}$) and YP-S_300 ($152 \text{ m}^2 \text{ g}^{-1}$, $0.12 \text{ cm}^3 \text{ g}^{-1}$) increase

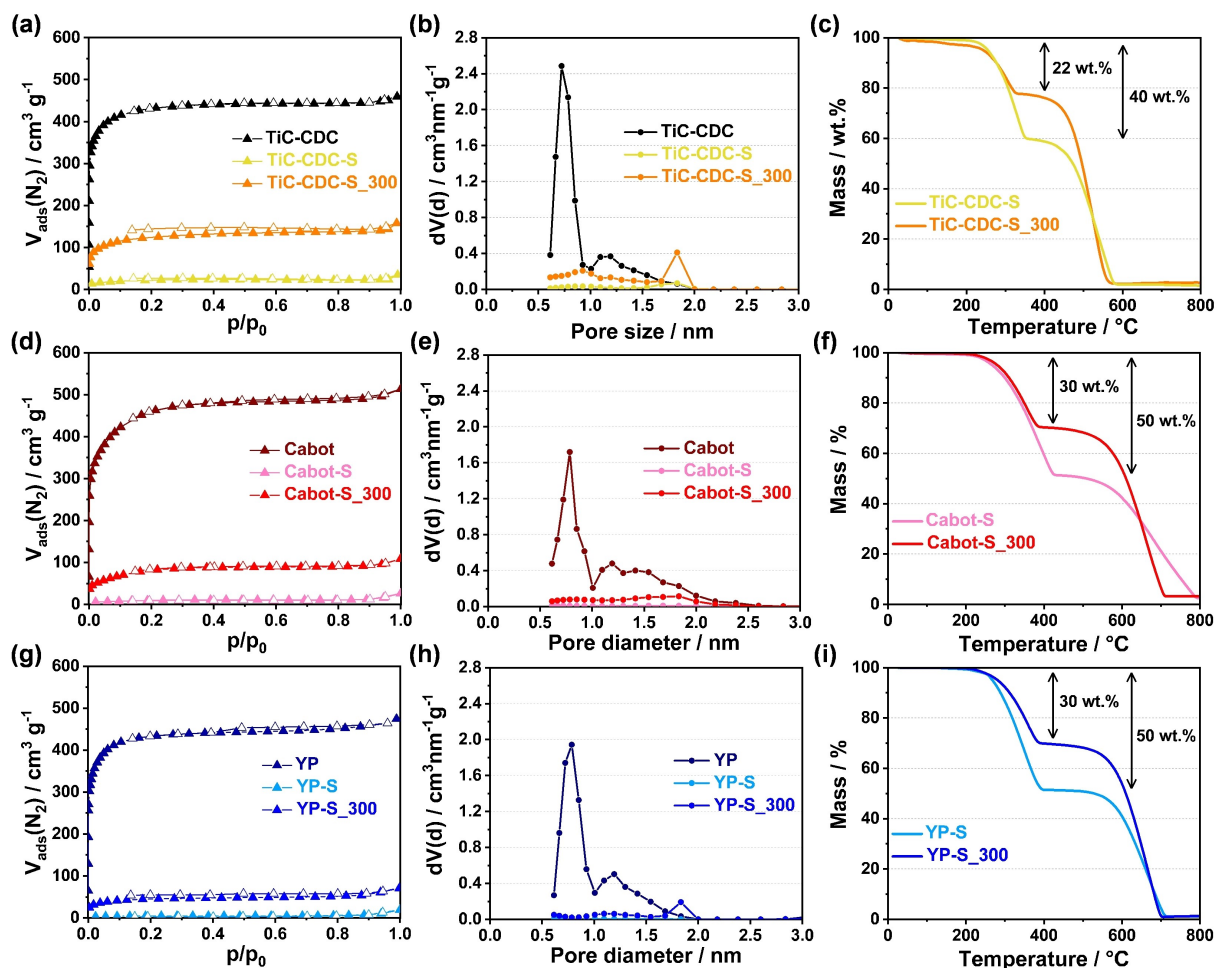


Figure 1. Nitrogen physisorption isotherms (a, d, g) and pore size distribution (b, e, h) determined by using QSDFT (slit pore, equilibrium model) of all samples. TG-curves of the corresponding C/S composites (c, f, i).

Table 1. Structural data of pristine, melt-infiltrated and evaporation treated sulfur samples: physisorption data derived from nitrogen isotherms measured at -196°C and sulfur contents determined by TG measurement using synthetic air.

Sample	$\text{SSA}_{\text{BET}}^{[a]} [\text{m}^2 \text{g}^{-1}]$	$V_{\text{tot}}(\text{N}_2)^{[b]} [\text{cm}^3 \text{g}^{-1}]$	$V_{\text{micro}}(\text{N}_2)^{[c]} [\text{cm}^3 \text{g}^{-1}]$	$W(\text{S})^{[d]} [\text{wt.\%}]$
TiC-CDC	1664	0.78	0.64	–
TiC-CDC-S	79	0.14	0.04	40
TiC-CDC-S_300	462	0.30	0.22	22
Cabot	1653	0.83	0.68	–
Cabot-S	35	0.06	0.01	50
Cabot-S_300	295	0.18	0.13	30
YP	1523	0.81	0.64	–
YP-S	15	0.06	0.01	50
YP-S_300	152	0.12	0.08	30

[a] SSA: specific surface area; calculated by using multipoint BET method for $0.05 \leq p/p_0 \leq 0.2$. [b] V_{tot} : total pore volume; determined at $p/p_0 = 0.99$. [c] V_{micro} : micropore volume; calculated by cumulative pore volume determined by QSDFT (slit pores, equilibrium model) for pores $< 2 \text{ nm}$. [d] Determined by TG analysis using synthetic air.

compared to the melt-infiltrated samples (Table 1). This effect is also observable in the PSDs (Figure 1(b) and Figure S1). This observation indicates that sulfur partially evaporates and all remaining sulfur is strongly bound inside the pores after this evaporation treatment.

Thermogravimetric (TG) analysis was carried out to investigate the sulfur contents of the various C/S-composites.

According to the TG data, the adjusted C:S ratios are confirmed for the melt-infiltration. Moreover, decreased sulfur contents of 22 wt% for TiC-CDC-S_300, 30 wt.% for Cabot-S_300 and YP-S_300 are determined for the evaporation treated composites containing only strongly bound sulfur.

An important question is the molecular structure of confined sulfur species. It is well known that elemental sulfur

shows characteristic polymorphism and undergoes various structural transitions during heating. At room temperature, the orthorhombic S_8 form (α -S) is thermodynamically stable. At 95.50°C the orthorhombic allotrope converts to monoclinic sulfur (β -S).^[42] Especially for molten sulfur, between its melting (119°C) and boiling point (293°C), various sulfur species (S_x , $x=5-33$) occur.^[13,42] In addition, at temperatures above 250°C the major fraction of sulfur vapor is in the form of S_{6-8} .^[42] However, DFT calculations suggest only short sulfur-chains (S_{2-4}) to fit into ultramicropores as their chain-like structure has at least one dimension below 0.50 nm, while the cyclo-sulfur molecule (S_{5-8}) exhibits diameter exceeding 0.50 nm (e.g. cyclo-octasulfur S_8 with a molecular diameter of approx. 0.84 nm).^[12,14] Furthermore, slit-shaped micropores of carbon materials are able to accommodate flat molecules, e.g. aromatic molecules. Therefore, it is assumed that S_8 rings can be adsorbed in slit-shaped pores due to their molecular geometry.^[24,43] Consequently, it is not entirely clear which sulfur species (linear or polymerized sulfur chains, cyclo-sulfur molecules or a mixture of them) are especially confined in micropores.

To obtain more insights into the nature of confined sulfur species, the corresponding composites were analyzed using X-ray absorption spectroscopy (XAS). In general, a XAS spectrum is divided in two areas, the X-ray absorption near edge structure (XANES) part which provides details on the oxidation state and the extended X-ray absorption fine-structure (EXAFS) part which reveals the atomic distribution.^[44]

In the sulfur K-edge XANES spectra two absorption features for all composites can be determined (Figure 2(a)). For comparison, a melt-infiltrated Ketjenblack/sulfur composite (KB-S) was also characterized as reference. All composites exhibit a significant signal at 2472 eV which is attributed to the transition from the S 1s to S-S π^* state of elemental sulfur.^[45] Further, a fairly wide as well as weak peak around 2479 eV is determined. This signal could be assigned to the S 1s transition to σ^* of COSO_2^- species.^[46,47] However, the EXAFS spectra of elemental sulfur reference (Figure S4) also exhibit this signal at the same energy and thus, the existence of the COSO_2^- species should be negligible. Nevertheless, this indicates that surface functionalities such as oxygen can be present within the carbon material. However, for the evaporation treated composites this peak is slightly wider or the signal exhibit an additional shoulder at 2482 eV, respectively (Figure S6). This shoulder might occur from the S 1s transition to σ^* of SO_4^{2-} species.^[47,48]

As the melt-infiltration was carried out in air a partial oxidation, especially terminated SO_x -groups cannot be excluded. In a previous study, covalent triazine frameworks with covalently bound sulfur were analyzed by means of XPS. In this work, additional peaks have been observed in the high resolution S 2p spectra and these signals were attributed to oxidized (terminal) sulfur species.^[49]

To clarify the structural environment around the absorbing sulfur atoms, the EXAFS spectra obtained by the CEY method were Fourier-transformed and the nearest-neighbor contributions were back-Fourier transformed into k -space. The EXAFS curve-fitting was carried out in the k space using a k^2 weighting scheme. For the fitting, only the S-S single scattering path was considered which resulted in the radial structure function (RSF) (Figure 2(b-d)). Moreover, the sulfur of KB-S sample was used as a reference for the calculations and thus, the corresponding parameters were assessed by fixing the coordination number N to a value of two ($N=2$), assuming S_8 ring molecules are present in the composite. According to the k window of the KB-S reference a significant peak at 1.75 Å with a slight shoulder at 1.29 Å (Figure 2(b)) is determined. Hence, a slight phase shift to lower distances is observed, while the exact S-S bond distance is 2.06 Å.^[50] Presumably, the carbon sulfur interaction or the Lennard-Jones potential of the micropore has an effect on the configuration of sulfur species and bond length, respectively. However, the applied EXAFS curve-fitting took the effect of phase shift into account. In contrast to the reference, the intensity of the signal at 1.75 Å is reduced and the shoulder at 1.35 Å is more pronounced for the evaporation-treated samples (Figure 2(c,d)). The lower intensity of the peak at 1.75 Å ($|X(R)| = 1.2$) could originate from a decreased coordination number or an increased Debye-Waller factor, respectively. Hence, an enhanced percentage of lower radial distance of the sulfur atoms can be assumed for the confined sulfur samples. This assumption is supported by the observed coordination numbers (N). As mentioned, the coordination number is fixed for KB-S reference material ($N=2$). However, the N values are slightly decreased to 1.84 (± 0.25) for Cabot-S_300 and 1.86 (± 0.20) for YP-S_300, respectively (Table 2). It can be concluded that a mixture of different sulfur molecules or a low concentration of sulfur forms, e.g. linear or polymerized chains are enclosed inside the micropores. However, the distribution of sulfur species can only be estimated. Unfortunately, TiC-CDC-S_300 has delivered noisy data due to residual

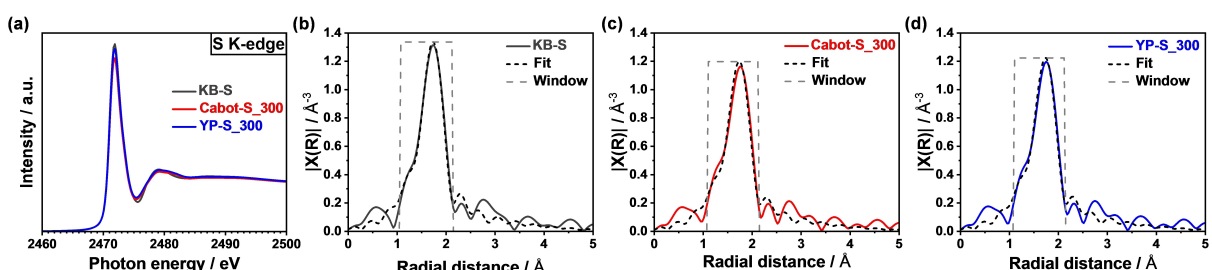


Figure 2. Sulfur K-edge XANES spectra of the evaporation treated microporous C/S composites and a melt-infiltrated Ketjenblack/sulfur reference (a) and the radial structure functions of the corresponding composites (b-d) obtained from the EXAFS spectra via the CEY method and the EXAFS curve-fittings.

Table 2. Summary of the fitting calculations of the EXAFS spectra. Errors of the parameters are given in parentheses.

Sample	Coordination number N	Distance r(S-S) [Å]
Cabot-S_300	1.84 (0.25)	2.06 (0.004)
YP-S_300	1.86 (0.20)	2.06 (0.003)
KB-S	2 [fixed]	2.06 (0.007)

chlorine impurities and therefore, a thorough analysis was not taken considered (Figure S7).

2.2. Electrochemical Performance in Coin Cells vs. Li/Li⁺

The three prototypical microporous carbon materials were studied as cathodes after confining the sulfur by a thermal treatment at 300 °C as described above. In particular, the initial and second cycle were investigated in regard of the irreversible capacity loss being caused by the reaction of polysulfides and carbonates. Subsequently, the cycle stability was analyzed. Eventually, the sulfur was solely infiltrated into the three microporous carbons, evaluated in terms of irreversible initial capacity loss as well as cycle stability, and compared with a micro-mesoporous reference material (Ketjenblack). Despite different sulfur contents of the cathodes (18.70 wt% for TiC-CDC and 25.50 wt% for activated carbons), comparable areal sulfur loadings of 1.50–1.70 mg_S cm⁻² were prepared. In order to ensure comparable test conditions, to ensure a complete wetting of the cathodes and sufficient sulfur utilization, the electrochemical experiments were carried out with a fixed electrolyte volume of 30 µl (TiC-CDC: E:S≈17.6, commercial

carbons: E:S≈15.1). The electrolyte amount plays a crucial role for the cell performance, especially for the sulfur utilization and cycling stability.^[3,51]

Figure 3 presents the voltage profiles and the corresponding cyclovoltammetry slopes of the first five cycles being obtained for the confined sulfur cathodes. In the first cycle, all samples show a minor plateau at 2.39 V, corresponding to the formation of long-chain polysulfide intermediates (Li₂S_x, x=6–8).^[8,16,30] Hence, residual sulfur (S₈) seems to be on the surface of the carbon particles or at the pore entrance after the evaporation process. The generated long-chain polysulfides react with carbonate molecules to thiocarbonates and hence, a portion of the sulfur (~150 mAh g_S⁻¹) is lost due to the irreversible reaction.^[16,27,29] Then, the voltage drops to 1.10 V for the activated carbon samples and 0.79 V for the TiC-CDC cathode. During the first discharge, a significant over-potential is observed for the quasi solid-to-solid conversion (~1.70 V).^[16,22,24,26] Moreover, high but irreversible discharge capacities of 2518 mAh g_S⁻¹, 3739 mAh g_S⁻¹ and 2737 mAh g_S⁻¹ are achieved for Cabot-S_300, TiC-CDC-S_300 and YP-S_300, respectively. In addition, the values of initial discharge capacities are much higher than the theoretical specific capacity of sulfur (1672 mAh g_S⁻¹). This can be an effect of a hindered sulfur conversion or side reactions, e.g. decomposition could take place during discharge process. After charging, a drastic loss of capacity (Cabot-S_300: 678 mAh g_S⁻¹, TiC-CDC-S_300: 682 mAh g_S⁻¹, YP-S_300: 896 mAh g_S⁻¹) is observed. In the further cycles, the capacity stabilizes and the typical plateaus (discharge: 1.66 V, charge: 2.30 V) for the quasi solid-to-solid conversion are detected. However, a slight overpotential and a reduced or slightly flattened plateau is

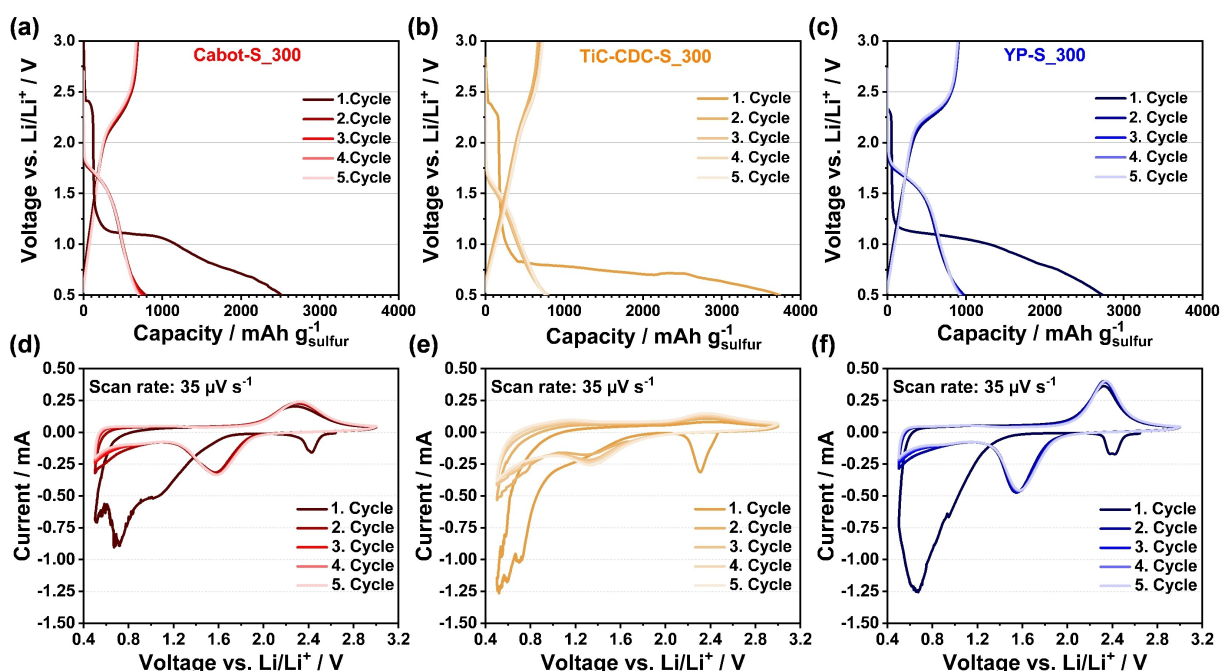


Figure 3. Voltage profiles (a-c) and CV-curves (d-f) of the evaporation treated composite cathodes for the first five cycles with an electrolyte volume 30 µl LP30 electrolyte. For galvanostatic testing a C-rate of C/10 and for CV measurements a scan rate of 35 µV s⁻¹ were utilized.

observed for TiC-CDC-S_300 sample. This effect can be attributed to the marginally narrow pore width of TiC-CDC scaffold (Table S1) and hence, enhanced polarization results from the Li^+ diffusion inside carbon matrix.^[14,31] The initial loss of capacity is a common phenomenon when carbonate-based electrolytes are used to discharge sulfur cathodes and is ascribed to the formation of an SEI-layer on cathode side, so called cathode-electrolyte interlayer-CEI.^[12,16,22,24] This CEI formation is also observed in the cyclic voltammograms (Figure 3(d-f)). All cathodes show three reduction peaks and one oxidation peak for the first scan corresponding to the plateaus being observed in the discharge slopes. Hence, the curves show the reaction of long chain polysulfide intermediates (~2.40 V) and the utilization of short-chain sulfur species (S_{2-4}) via a quasi-solid-to-solid mechanism (~1.60 V).^[8,24] Additionally, a remarkable peak at ~0.69 V is determined for all samples which is attributed to a decomposition process. It is known that ethylene carbonate (EC) in the LP30 electrolyte decomposes at 0.65 V (vs. Li/Li⁺) on a carbon working electrode.^[52] As a result, a protective CEI is generated on the cathode surface, which is expected to encapsulate the sulfur inside the pores. Various surface studies have recently shown that sulfur can be encapsulated in the pores below the CEI layer.^[16,24,26,27] Hence, active material is irreversibly consumed during the CEI formation and cannot be electrochemically utilized in the subsequent cycles. Moreover, the intercalation of Li^+ ions during the discharge process into graphitized segments could also take place contributing to the high initial discharge capacities.^[53]

Further electrochemical experiments on TiC-CDC cathodes were carried out by varying the voltage window and C-rates of the discharge to investigate the role of the CEI for the cycling performance. Figure 4(a) shows the impact of varying cut-off voltage affecting the 1st and 2nd cycle for Ti-CDC as sulfur host. At a higher cut-off voltage of 1.20 V (vs. Li/Li⁺) no CEI generation is observed and hence, nearly no sulfur utilization is achieved for the further cycles. When a potential window of 0.50–3.00 V vs. Li/Li⁺ is applied for the initial cycle, a moderate sulfur utilization is determined by using reduced potential window of 1.00–3.00 V (vs. Li/Li⁺) for cycling. However, the

slopes show a lowered voltage curve due to a slightly increasing over-potential (Figure 4(b)). Since a protective SEI layer on cathode surface is generated, additional resistance and polarization effects arise during cycling.^[21,25,54] In this regard, the lithium diffusion through the SEI layer is presumably hindered and leads to reduced sulfur utilization. Consequently, the confined sulfur cathode was cycled with varying lower C-rates (C/20 and C/50) after the formation at C/10 to investigate the influence of the C-rate on the polarization and utilization. When using lower C-rates after the initial formation, the discharge slopes show an evolving plateau below 0.70 V as more time is provided for the overall reaction, including undesired decomposition processes. Hence, similar cycle performance and sulfur utilization is observed for C/20 and C/50 compared to the initially applied C/10 (Figure S9). Consequently, the negligible effect of the C-rate on the CEI formation and sulfur utilization is confirmed for a microporous carbon containing predominantly supermicropores.^[26]

Figure 5 shows the electrochemical performance and the corresponding voltage profiles of all confined sulfur cathodes with LP30 electrolyte for cycle 5 and the following. All cathodes reveal discharge capacities over 797 mAh g_{sulfur}⁻¹ and show comparable capacity retention. The YP-S_300 sample exhibits slightly higher discharge capacities in the first 80 cycles compared to the other cathodes. Hence, after 100 cycles 515 mAh g_{sulfur}⁻¹ (102.2% CE), 538 mAh g_{sulfur}⁻¹ (101.7% CE), 536 mAh g_{sulfur}⁻¹ (100.2% CE) for Cabot-S_300, YP-S_300 and TiC-CDC-S_300 are achieved, respectively. Moreover, all samples show a nearly linear degradation and hence, after 200 cycles comparable discharge capacities below 350 mAh g_{sulfur}⁻¹ are observed. The corresponding voltage profiles of the electrodes are demonstrated in Figure 5 (b-d). All samples show the typical slopes for quasi-solid-state mechanism with a single discharge plateau at 1.66 V and charge plateau at 2.30 V, corresponding to the reduction and oxidation of small chain polysulfides (Li_xS_x , $x=2-4$).^[11-28] However, a slight over-potential (<1.60 V) and a reduced or more flatten plateau are determined for TiC-CDC-S_300 sample. This effect can be attributed to the marginally narrow pore width of TiC-CDC scaffold (Table S1) and hence, enhanced polarization during the Li^+ diffusion inside carbon

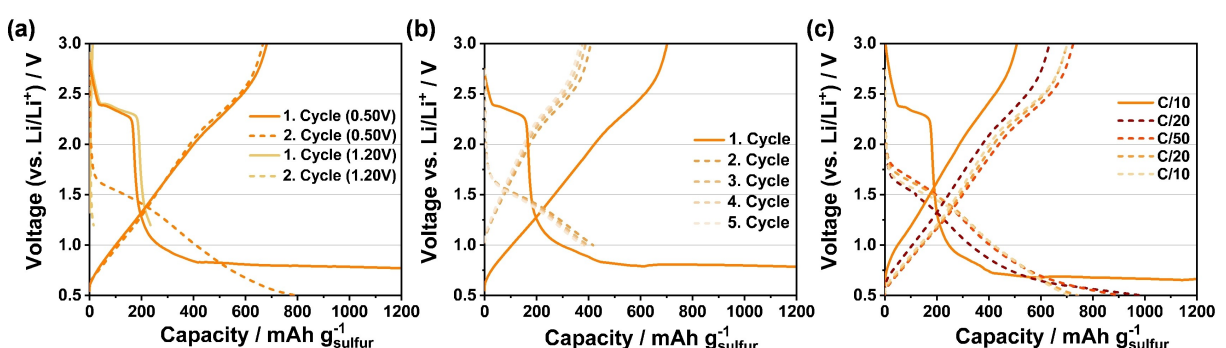


Figure 4. First discharge and charge profiles of cells with TiC-CDC-S_300 cathode cycled under different electrochemical test conditions: a) potential window of 0.50–3.00 V and 1.20–3.00 V vs. Li/Li⁺ at C/10, b) first cycle at 0.50–3.00 V and further cycling at 1.00–3.00 V vs. Li/Li⁺ at C/10, c) first cycle at C/10 and afterwards lower discharge C-rates at 0.50–3.00 V vs. Li/Li⁺.

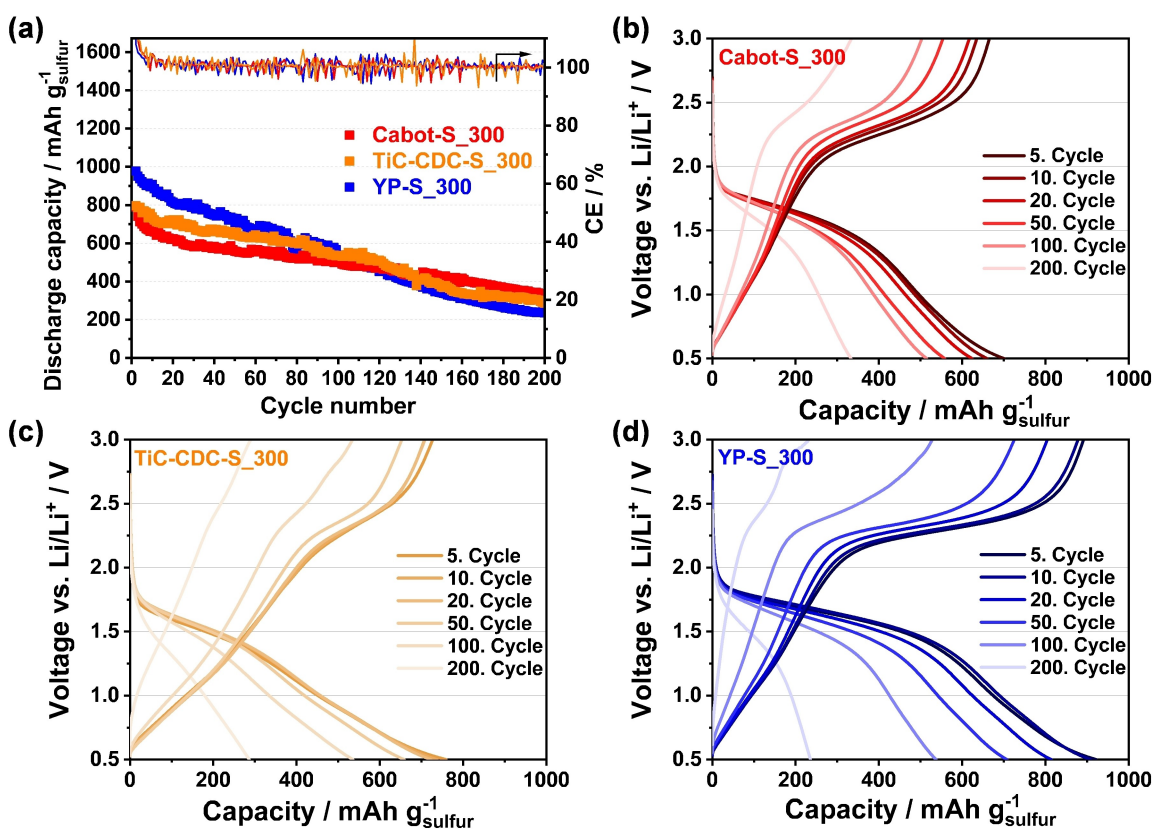


Figure 5. Galvanostatic cycling performance (a) and corresponding voltage profiles (b-d) of the evaporation treated C/S-composite cathodes at C/10 with an electrolyte volume of 30 μL LP30 electrolyte.

matrix.^[14,31] Furthermore, a coulombic efficiency more than 100% is observed, especially within the first 10 cycles. This phenomenon is attributed to the CEI formation and electrolyte decomposition during the discharge process.

However, for all evaporation treated cathodes only about half of the theoretical capacity (Cabot: 48%, TiC-CDC: 48%, YP: 58%) is utilized, despite the sulfur is confined in the micropores. This might be attributed the sulfur loss during the CEI formation process. Thus, the calculated capacity and the applied C-rate are higher for the residual active material and lead to reduced sulfur utilizations. Besides, by employing standard ether-based electrolyte with LiNO₃ as additive (Figure S10) enhanced sulfur utilization (Cabot: 1086 mAh g_s⁻¹, TiC-CDC: 1031 mAh g_s⁻¹, YP: 1312 mAh g_s⁻¹) is observed as the irreversible active material loss due to the reaction with carbonates does not take place. However, the theoretical capacity is not achieved due to the well-known technological issues of solid-liquid-solid conversion.^[8-10] Since the generation of the CEI seems to be crucial for a stable cycling in carbonate-based electrolytes, non-evaporation treated C/S composites and a standard carbon black were electrochemical analyzed (Figure 6). Here, a clear difference between the carbon materials and their porosity properties was observed.

Discharge capacities above the theoretical value (1744 mAh g_s⁻¹, 1599 mAh g_s⁻¹, 1856 mAh g_s⁻¹ for Cabot-S, TiC-CDC-S and YP-S, respectively) are again achieved. Surprisingly,

after the first cycle, a moderate cycle performance and reduced sulfur utilization is still determined for the microporous cathodes (Figure S11). According to the voltage profiles, a short discharge plateau at 2.30 V is also observed due to the formation of long-chain polysulfide intermediates (Li₂S₆₋₈).^[8,30] A second discharge plateau at 1.33 V for activated carbons and 0.78 V for TiC-CDC corresponding to the utilization of short-chain sulfur species (S₂₋₄) via quasi solid-state mechanism is also achieved. Moreover, the over-potential of the quasi solid-solid conversion plateau seems to be decreased during the process until it increases again. However, the sulfur utilization and cycle performance is reduced compared to the evaporation treated cathode composites containing strongly bound sulfur. In this regard, after 5 cycles comparably low discharge capacities of 443 mAh g_s⁻¹, 440 mAh g_s⁻¹, 621 mAh g_s⁻¹ for Cabot-S, TiC-CDC-S and YP-S are obtained, respectively. Presumably, more active material is lost during the formation of the protective CEI layer, while a certain percentage (~40%) of the sulfur maintains at the surface of the carbon particles after melt-infiltration (Figure 7). Consequently, active material is consumed to a higher degree during CEI formations.

We also compared a reference Ketjenblack/sulfur cathode analyzing operation in the carbonate-based electrolyte. In contrast to the microporous scaffolds, the Ketjenblack cathode shows no meaningful utilization in LP30 electrolyte. Only in the first discharge an irreversible capacity of 789 mAh g_s⁻¹ is

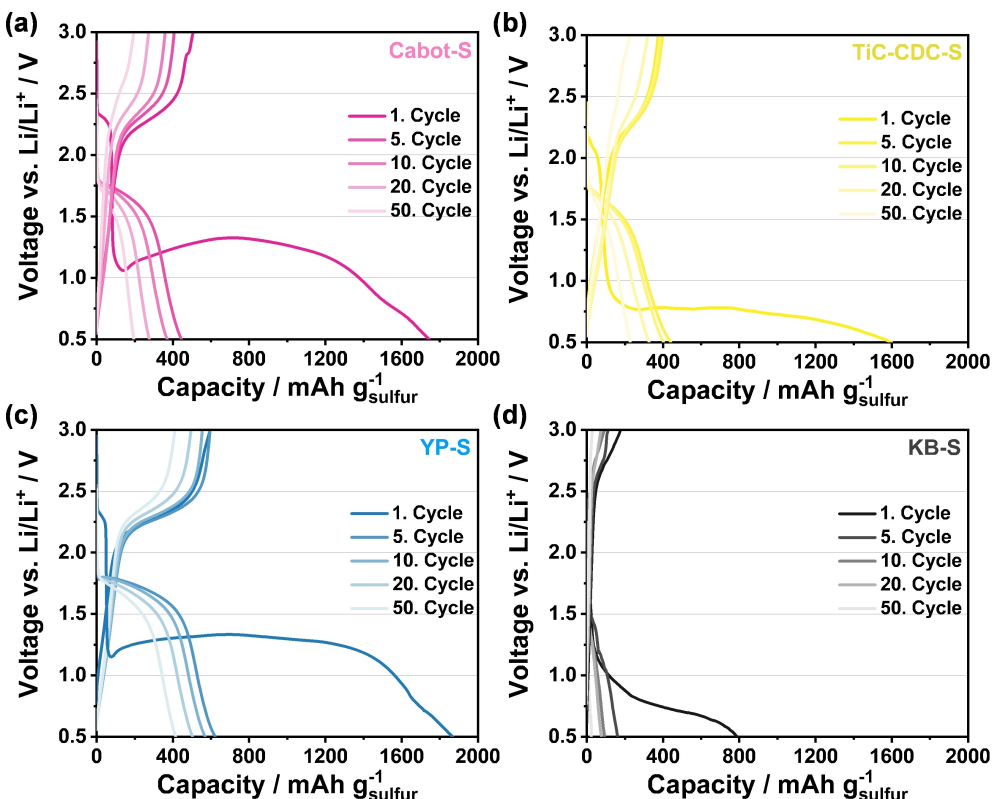


Figure 6. Voltage profiles of only melt-infiltrated microporous C/S composites (a–c) and a Ketjenblack/sulfur reference (d) at C/10 with an electrolyte volume of 30 μ l LP30 electrolyte.

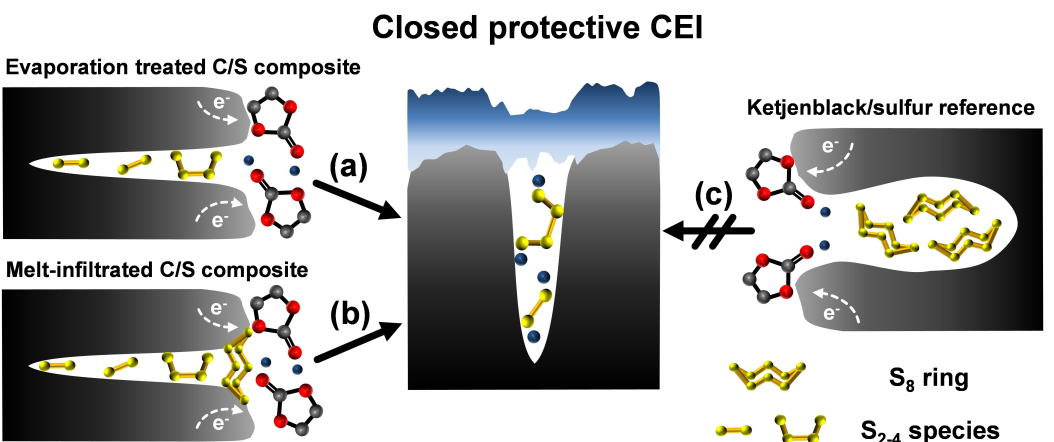


Figure 7. Schematic illustration of the respective cathode material during initial discharge process or CEI formation: a) evaporation treated C/S composite, b) melt-infiltrated C/S composite and c) Ketjenblack/sulfur reference as Li-S cathodes in carbonate-based LP30 electrolyte.

detected which is mainly attributed to the electrolyte decomposition below 0.65 V (Figure 6(d)). After the first cycle, the capacity decreases to values below 175 mAh g⁻¹ and poor cycle performance is determined. This, indicates a protective closed CEI layer cannot form because of the large pore size and small particle size of Ketjenblack. This hierarchical porous carbon black consists of mainly of micron sized highly porous particles forming agglomerates with additional interparticle

mesopores (Figure S2) and hence, the pore openings of the particles and interparticle pores are too large to form a closed protective CEI layer (Figure 7).

Hence, we conclude the formation of a protective CEI layer on the cathode surface to be a fundamental requirement to utilize sulfur in the presence of carbonate-based electrolytes in Li-S batteries. The microporous carbon encapsulates the sulfur, and the small pore opening in combination with large particle

size promotes the formation of a closed protective CEI. Our results suggest the encapsulation of shorter chain sulfur species (S_2 , S_4 or alike) as frequently assumed to be required for the quasi solid-state conversion mechanism promoted by micro-porous carbons, not to be a necessary condition for operating sulfur cathodes in carbonate based electrolytes.^[24] Instead, our findings indicate the porosity characteristics mainly to be responsible for variations in CEI formation mechanisms. In particular microporous carbons enable the formation of a closed protective CEI layer.

3. Conclusions

Several microporous ($d < 2$ nm) and mesoporous model carbon materials were studied as sulfur cathode materials in operation with carbonate based electrolyte to understand the role of sulfur confinement and synergistic SEI formation on the cathode. After melt-infiltration an additional evaporation treatment at 300 °C was performed in order to ensure that only strongly bound, trapped sulfur species remain inside the micropores. Despite the resulting composites contain lower sulfur fractions (22 wt% and 30 wt%) than the melt-infiltrated C/S-composites, the performance of the evaporation treated cathodes is clearly superior in LP30, revealing stable cycling up to 200 cycles as well as a quasi-solid-to-solid mechanism for all cathodes with this highly confined sulfur. CV experiments indicate only a slight loss of active material during the initial discharge due to irreversible reaction with carbonate molecules as well as the generation of a protective closed CEI layer on the cathode surface of microporous carbons originating from carbonate electrolyte decomposition. This initial loss in utilization is more pronounced in non-evaporation treated micro-porous electrodes suggesting sulfur species in interparticular pores or residual mesopores of the predominantly microporous carbons, which are less strongly bound, to be responsible for irreversible side reactions with the carbonates causing cell failure. A purely mesoporous reference electrode based on Ketjenblack instead shows no active material utilization and poor cycle performance in LP30 electrolyte as it cannot form a closed protective CEI layer. EXAFS spectra of confined sulfur species in evaporation treated microporous carbons reveal an average coordination number only slightly below 2, indicating only a small fraction of short chain sulfur species (S_2, S_4), if at all, to be confined in the micropores. These findings suggest the main role of small pore diameter porous carbons is to enable the formation of a closed protective CEI layer on the carbon grains rather than promoting the formation of short chain sulfur species inside as a necessary requirement for reversible operation. The observed variations in CEI formation provide a new mechanistic view on the operation of Li-S battery cathodes and are important for designing cathodes that enable the application of a wider range of commercially established electrolytes in future.

Experimental Section

Carbon materials

Titanium carbide-derived-carbon (TiC-CDC) was prepared from crystalline TiC powder (Sigma Aldrich, ≥99%, <4 µm) using high temperature (1000 °C) chlorination reported elsewhere.^[55] For comparison, two commercially available activated carbon materials with comparable microporous features, namely Cabot (purchased from Cabot Norit Nederland B.V) and YP (purchased from Kuraray Chemical Co., Ltd) were additionally investigated. As a reference, the micro/mesoporous carbon black material Ketjenblack EC-600JD (purchased from Akzonobel) was employed.

Synthesis of C/S composites

The C/S composites were synthesized by using a melt-filtration process followed by an evaporation procedure. Before sulfur infiltration, all microporous carbon materials were activated at 200 °C for 12 h under vacuum. The Ketjenblack reference was dried at 120 °C. The dried carbons were mixed with pristine sulfur (Carl Roth, >99.50%) in varying mass ratios and heated up to 155 °C for 12 h under ambient conditions. The following evaporation process was carried out in a quartz tube furnace (Ø: 40 mm) at 300 °C for 2 h under argon atmosphere (0.4 slm). During the heat treatment, an initial heating rate of 5 °C min⁻¹ and above 150 °C, a slow heating rate of 1 °C min⁻¹ was used.

Electrode preparation

Li-S cathodes were prepared using a manual solvent-free procedure as described elsewhere.^[56] The as-prepared C/S composites were mixed with multi-walled carbon nanotubes (MWCNT, Nanocyl 7000) and poly(tetrafluoroethylene) (PTFE) binder in a weight ratio of 85:12:3. After homogenization and intensive grinding, electrode sheets were prepared using shearing forces. Afterwards, the free-standing cathode films were laminated onto a primer-coated aluminum current collector for electrochemical characterization. For coin cell testing, cathodes were punched into circular electrodes (diameter: 12 mm) with sulfur loadings of approx. 1.70 ± 0.20 mg_s cm⁻² and electrode densities of approx. 0.60 ± 0.05 g cm⁻³.

Structural characterization

Nitrogen physisorption measurements were performed at -196 °C on a Rubotherm BELSORP after degassing the samples under vacuum. The pristine carbons were heated for 12 h at 200 °C and sulfur loaded samples were activated at room temperature. Specific surface areas were calculated based on multi-point Brunauer-Emmett-Teller (BET) method in the range of 0.05–0.20 p/p₀. The values of the total pore volume were determined at relative pressure p/p₀ = 0.99. Micropore volumes were calculated from the cumulative pore volumes at a diameter of 2 nm using the Quenched-Solid-Density-Functional-Theory (QSDFT) calculation for carbon (slit pores, adsorption branch kernel).

Raman spectroscopy data were collected using a Renishaw *inVia* Raman spectrometer under ambient conditions and a laser excitation wavelength of 514 nm. By determining the ratio of the peak intensities I_D/I_G , the intensities of the D- and the G-band were calculated by fitting the spectra with a Lorentzian function using OriginLab® 2016.

Thermal analysis was conducted with a Netzsch STA 409 PC LUXX with a heating rate of 5 K min⁻¹ under synthetic air conditions.

The morphology of carbon materials was characterized by Scanning Electron Microscopy (SEM) on a SU8020 (Hitachi) with a triple detector system for secondary and low-energy backscattered electrons operating with an acceleration voltage of 4 kV. Prior to measurement, the samples were fixed on a carbon pad.

The Sulfur K-edge EXAFS measurements were performed at BL6N1 beamline of Aichi Synchrotron Radiation Center equipped with a InSb(111) double-crystal monochromator. All spectra in the range 2400–3200 eV were simultaneously collected in conversion electron yield (CEY) mode and partial fluorescence yield (PFY) mode. For CEY, a bias voltage of +150 V was applied to a Cu-grid in front of a sample holder. The PFY signal was detected by a single-element silicon drift detector (SDD, Hitachi High Technologies Science America, Vortex-EM). The incidence angle of X-ray was set to 20°, and the direction of PFY detection was perpendicular to the incident X-ray and parallel to its polarization vector. The samples were attached to carbon tape and were set in a chamber under helium atmosphere. The EXAFS data reduction and analysis were performed with the Athena/Artemis software package.^[57] The EXAFS spectra obtained by the CEY method were Fourier transformed in the *k* range between 4.3–12.7 Å⁻¹, and the nearest-neighbor contributions (1.05–2.14 Å) were back-Fourier transformed into *k*-space. The EXAFS curve-fitting was made in the *q* space using a *k*² weighting scheme and only the S-S single scattering path was considered for the fitting. The sulfur on a Ketjenblack/sulfur sample was used as a reference, and amplitude reduction factor ($S_0^{(2)}$), relative shift in ionization energy (ΔE_0), Debye-Waller factor (σ^2), and distance (*R*) were assessed by fixing the coordination number (*N*) to *N*=2, assuming a ring polymer S₈ molecule. As for the other samples, the σ^2 , *R*, and *N* parameters were evaluated by fixing the $S_0^{(2)}$ and ΔE_0 values to the ones obtained for the sulfur on Ketjenblack/sulfur composite.

Cell assembly and electrochemical characterization

All C/S cathodes were dried at 50 °C for 1 h under vacuum prior to cell assembly (CR2016, MTI Corp.). The Li-S half cells were assembled by stacking the corresponding cathode, a PE separator (diameter: 19 mm, thickness: 12 µm) and an elemental lithium chip (MTI Corp., diameter: 16.5 mm, thickness: 250 µm) in an Argon-filled glove box (MBraun, conditions: <0.1 ppm O₂ and H₂O). Before sealing, a defined volume of 30 µl of carbonate-based LP30 electrolyte (1 M LiPF₆ in EC/DMC (v:v=1:1)) was added.

All electrochemical measurements were performed at constant laboratory temperature (22±2 °C). The capacity and long-term stability of the cells was characterized by galvanostatic cycling with a battery tester CTS-Lab (BaSyTec). The Li-S cells were operated at a constant rate of C/10 (1 C=1672 mAh g⁻¹) in a voltage range of 0.50–3.00 V vs. Li/Li⁺. The Coulombic efficiency (CE) was determined by dividing the discharge (lithiation) capacity by the charge (delithiation) capacity. Cyclic voltammograms were measured using a VSP-300 multichannel potentiostat/galvanostat (Bio-Logic). Scans were performed in a voltage range of 0.50–3.00 V vs. Li/Li⁺ with a scan rate of 35 µV s⁻¹ (corresponding to a C-rate of approx. C/20).

Acknowledgements

This work has received funding from the Federal Ministry of Education and Research (BMBF), Japanese-German Cooperation on Battery project, supporting code 03XP0229 C ("AReLiS"). The authors acknowledge Friedrich Schwotzer (TU-Dresden) for the

SEM images. Open access funding enabled and organized by Projekt DEAL.

Conflict of Interest

The authors declare no conflict of interest.

Keywords: lithium-sulfur battery • confined sulfur • cathode-electrolyte interphase • microporous carbon • porosity influence

- [1] a) P. G. Bruce, S. A. Freunberger, L. J. Hardwick, J.-M. Tarascon, *Nat. Mater.* **2011**, *11*, 19–29; b) A. Rosenman, E. Markevich, G. Salitra, D. Aurbach, A. Garsuch, F. F. Chesneau, *Adv. Energy Mater.* **2015**, *5*, 1500212; c) A. Fotouhi, D. Auger, L. O'Neill, T. Cleaver, S. Walus, *Energies* **2017**, *10*, 1937; d) R. Kumar, J. Liu, J.-Y. Hwang, Y.-K. Sun, *J. Mater. Chem. A* **2018**, *6*, 11582–11605.
- [2] a) X. Ji, L. F. Nazar, *J. Mater. Chem.* **2010**, *20*, 9821; b) X.-B. Cheng, R. Zhang, C.-Z. Zhao, Q. Zhang, *Chem. Rev.* **2017**, *117*, 10403–10473; c) T. Cleaver, P. Kovacic, M. Marinescu, T. Zhang, G. Offer, *J. Electrochem. Soc.* **2018**, *165*, A6029–A6033.
- [3] S. Dörfler, H. Althues, P. Härtel, T. Abendroth, B. Schumm, S. Kaskel, *Joule* **2020**, *4*, 539–554.
- [4] a) Q. Pang, X. Liang, C. Y. Kwok, L. F. Nazar, *Nat. Energy* **2016**, *1*, 652; b) G. Li, S. Wang, Y. Zhang, M. Li, Z. Chen, J. Lu, *Adv. Mater.* **2018**, *30*, e1705590; c) X. Wang, Y. Tan, G. Shen, S. Zhang, *J. Energy Chem.* **2020**, *41*, 149–170; d) X.-B. Cheng, J.-Q. Huang, Q. Zhang, *J. Electrochem. Soc.* **2018**, *165*, A6058–A6072; e) Y. Diao, K. Xie, S. Xiong, X. Hong, *J. Power Sources* **2013**, *235*, 181–186; f) A. F. Hofmann, D. N. Fronczeck, W. G. Bessler, *J. Power Sources* **2014**, *259*, 300–310.
- [5] a) C. Weller, S. Thieme, P. Härtel, H. Althues, S. Kaskel, *J. Electrochem. Soc.* **2017**, *164*, A3766–A3771; b) C. Weller, J. Pampel, S. Dörfler, H. Althues, S. Kaskel, *Energy Technol.* **2019**, *7*, 1900625; c) Q. Pang, A. Shyamsunder, B. Narayanan, C. Y. Kwok, L. A. Curtiss, L. F. Nazar, *Nat. Energy* **2018**, *3*, 783–791; d) M. Yanagi, K. Ueno, A. Ando, S. Li, Y. Matsumae, J. Liu, K. Dokko, M. Watanabe, *J. Electrochem. Soc.* **2020**, *167*, 70531.
- [6] a) Y. Li et al., *Chem. Eng. J.* **2020**, *380*, 122595; b) Z. Wie Seh, W. Li, J. J. Cha, G. Zheng, Y. Yang, M. T. McDowell, P.-C. Hsu, Y. Cui, *Nat. Commun.* **2013**, *4*, 1331; c) X. Liang et al., *Adv. Energy Mater.* **2016**, *6*, 1501636; d) Z. Li, H. Jiang, N.-C. Lai, T. Zhao, Y.-C. Lu, *Chem. Mater.* **2019**, *31*, 10186–10196; e) S. Mei, C. J. Jafta, I. Lauermann, Q. Ran, M. Kärgell, M. Ballauff, Y. Lu, *Adv. Funct. Mater.* **2017**, *27*, 1701176.
- [7] a) S. Dörfler et al., *Nano Energy* **2018**, *54*, 116–128; b) C. Schneidermann, C. Kensy, P. Otto, S. Oswald, L. Giebel, D. Leistenschneider, S. Grätz, S. Dörfler, S. Kaskel, L. Borchardt, *ChemSusChem* **2019**, *12*, 310–319; c) C. Kensy, P. Härtel, J. Maschita, S. Dörfler, B. Schumm, T. Abendroth, H. Althues, B. V. Lotsch, S. Kaskel, *Carbon* **2020**, *161*, 190–197.
- [8] M. Wild, L. O'Neill, T. Zhang, R. Purkayastha, G. Minton, M. Marinescu, G. J. Offer, *Energy Environ. Sci.* **2015**, *8*, 3477–3494.
- [9] M. Marinescu, L. O'Neill, T. Zhang, S. Walus, T. E. Wilson, G. J. Offer, *J. Electrochem. Soc.* **2018**, *165*, A6107–A6118.
- [10] J. Liu, H. Chen, W. Chen, Y. Zhang, Y. Zheng, *ChemElectroChem* **2019**, *6*, 2782–2787.
- [11] B. Zhang, X. Qin, G. R. Li, X. P. Gao, *Energy Environ. Sci.* **2010**, *3*, 1531.
- [12] S. Xin, L. Gu, N.-H. Zhao, Y.-X. Yin, L.-J. Zhou, Y.-G. Guo, L.-J. Wan, *J. Am. Chem. Soc.* **2012**, *134*, 18510–18513.
- [13] S. S. Zhang, *Front. Energy Res.* **2013**, *1*, 1–9.
- [14] W. Zhang, D. Qiao, J. Pan, Y. Cao, H. Yang, X. Ai, *Electrochim. Acta* **2013**, *87*, 497–502.
- [15] Z. Li, L. Yuan, Z. Yi, Y. Sun, Y. Liu, Y. Jiang, Y. Shen, Y. Xin, Z. Zhang, Y. Huang, *Adv. Energy Mater.* **2014**, *4*, 1301473.
- [16] Y. Xu, Y. Wen, Y. Zhu, K. Gaskell, K. A. Cychosz, B. Eichhorn, K. Xu, C. Wang, *Adv. Funct. Mater.* **2015**, *25*, 4312–4320.
- [17] T. Takahashi, M. Yamagata, M. Ishikawa, *Prog. Nat. Sci.* **2015**, *25*, 612–621.
- [18] C. Fu, B. M. Wong, K. N. Bozhilov, J. Guo, *Chem. Sci.* **2016**, *7*, 1224–1232.
- [19] J. T. Lee, K. Eom, F. Wu, H. Kim, D. C. Lee, B. Zdryko, G. Yushin, *ACS Energy Lett.* **2016**, *1*, 373–379.

- [20] S. Niu, G. Zhou, W. Lv, H. Shi, C. Luo, Y. He, B. Li, Q.-H. Yang, F. Kang, *Carbon* **2016**, *109*, 1–6.
- [21] A. Rosenman, E. Markevich, G. Salitra, Y. Talyosef, F. Chesneau, D. Aurbach, *J. Electrochem. Soc.* **2016**, *163*, A1829–A1835.
- [22] Q. Zhu, Q. Zhao, Y. An, B. Anasori, H. Wang, B. Xu, *Nano Energy* **2017**, *33*, 402–409.
- [23] L. Hu, Y. Lu, X. Li, J. Liang, T. Huang, Y. Zhu, Y. Qian, *Small* **2017**, *13*.
- [24] E. Markevich, G. Salitra, Y. Talyosef, F. Chesneau, D. Aurbach, *J. Electrochem. Soc.* **2017**, *164*, A6244–A6253.
- [25] M. Helen, T. Diemant, S. Schindler, R. J. Behm, M. Danzer, U. Kaiser, M. Fichtner, M. Anji Reddy, *ACS Omega* **2018**, *3*, 11290–11299.
- [26] M. Helen, M. Fichtner, M. A. Reddy, *Energy Technol.* **2019**, *7*, 1900183.
- [27] L. Wang, Y. Lin, S. DeCarlo, Y. Wang, K. Leung, Y. Qi, K. Xu, C. Wang, B. W. Eichhorn, *Chem. Mater.* **2020**.
- [28] X. Li et al., *Nat. Commun.* **2018**, *9*, 4509.
- [29] T. Yim et al., *Electrochim. Acta* **2013**, *107*, 454–460.
- [30] C. Barchasz, F. Molton, C. Duboc, J.-C. Leprétre, S. Patoux, F. Alloin, *Anal. Chem.* **2012**, *84*, 3973–3980.
- [31] D.-W. Wang, Q. Zeng, G. Zhou, L. Yin, F. Li, H.-M. Cheng, I. R. Gentle, G. Q. M. Lu, *J. Mater. Chem. A* **2013**, *1*, 9382.
- [32] a) Z. Lin, Z. Liu, W. Fu, N. J. Dudney, C. Liang, *Angew. Chem. Int. Ed.* **2013**, *52*, 7460–7463; *Angew. Chem.* **2013**, *125*, 7608–7611; b) U. Ulissi, S. Ito, S. M. Hosseini, A. Varzi, Y. Aihara, S. Passerini, *Adv. Energy Mater.* **2018**, *8*, 1801462.
- [33] a) J. Fanous, M. Wegner, J. Grimminger, Ä. Andresen, M. R. Buchmeiser, *Chem. Mater.* **2011**, *23*, 5024–5028; b) S. Zhang, *Energies* **2014**, *7*, 4588–4600; c) S. Warneke, R. K. Zenn, T. Lebherz, K. Müller, A. Hintennach, U. Starke, R. E. Dinnebier, M. R. Buchmeiser, *Adv. Sustainable Syst.* **2018**, *2*, 1700144.
- [34] X. Chen et al., *Nat. Commun.* **2019**, *10*, 1021.
- [35] D.-W. Wang, G. Zhou, F. Li, K.-H. Wu, G. Q. M. Lu, H.-M. Cheng, I. R. Gentle, *Phys. Chem. Chem. Phys.* **2012**, *14*, 8703–8710.
- [36] E. Markevich, G. Salitra, A. Rosenman, Y. Talyosef, F. Chesneau, D. Aurbach, *Electrochem. Commun.* **2015**, *60*, 42–46.
- [37] V. Presser, M. Heon, Y. Gogotsi, *Adv. Funct. Mater.* **2011**, *21*, 810–833.
- [38] E. Zera, W. Nickel, G. P. Hao, L. Vanzetti, S. Kaskel, G. D. Sorarù, *J. Mater. Chem. A* **2016**, *4*, 4525–4533.
- [39] M. Oschatz, P. Pré, S. Dörfler, W. Nickel, P. Beaunier, J.-N. Rouzaud, C. Fischer, E. Brunner, S. Kaskel, *Carbon* **2016**, *105*, 314–322.
- [40] M. Thommes, K. Kaneko, A. V. Neimark, J. P. Olivier, F. Rodriguez-Reinoso, J. Rouquerol, K. S. W. Sing, *Pure Appl. Chem.* **2015**, *87*, 1051–1069.
- [41] a) A. C. Ferrari, J. Robertson, *Phys. Rev. B* **2000**, *61*, 14095–14107; b) A. C. Ferrari, *Solid State Commun.* **2007**, *143*, 47–57.
- [42] B. Meyer, *Chem. Rev.* **1976**, *76*, 367–388.
- [43] K. S. W. Sing, R. T. Williams, *Part. Part. Syst. Charact.* **2004**, *21*, 71–79.
- [44] D. C. Koningsberger, R. Prins, *X-ray absorption. Principles, applications, techniques of EXAFS, SEXAFS, and XANES*, Wiley, New York, **1988**, Vol. 92.
- [45] a) European Synchrotron Radiation Facility (ESRF), "Database inorganic sulfur compounds. Sulfur", to be found under <https://www.esrf.eu/home/UsersAndScience/Experiments/XNP/ID21/php/Database-SCompounds.html>; b) J. M. Durand, J. Olivier-Fourcade, J. C. Jumas, M. Womes, C. M. Teodorescu, A. Elafif, J. M. Esteva, R. C. Karnatak, *J. Phys. B: At. Mol. Opt. Phys.* **1996**, *29*, 5773–5784.
- [46] A. Dey et al., *J. Am. Chem. Soc.* **2006**, *128*, 533–541.
- [47] X. Feng, M.-K. Song, W. C. Stolte, D. Gardenghi, D. Zhang, X. Sun, J. Zhu, E. J. Cairns, J. Guo, *Phys. Chem. Chem. Phys.* **2014**, *16*, 16931–16940.
- [48] D. A. McKeown, I. S. Muller, H. Gan, I. L. Pegg, W. C. Stolte, *J. Non-Cryst. Solids* **2004**, *333*, 74–84.
- [49] E. Troschke, C. Kensy, F. Haase, S. Dörfler, Y. Joseph, B. V. Lotsch, S. Kaskel, *Batteries & Supercaps* **2020**, *3*, 1069–1079; *Supercaps* **2020**, *3*, 1069–1079.
- [50] R. Steudel, *Angew. Chem. Int. Ed. Engl.* **1975**, *14*, 655–664.
- [51] S. Chen et al., *Joule* **2019**, *3*, 1094–1105.
- [52] V. Sharova, A. Moretti, T. Diemant, A. Varzi, R. J. Behm, S. Passerini, *J. Power Sources* **2018**, *375*, 43–52.
- [53] M. Winter, J. O. Besenhard, M. E. Spahr, P. Novák, *Adv. Mater.* **1998**, *10*, 725–733.
- [54] X.-B. Cheng, R. Zhang, C.-Z. Zhao, F. Wei, J.-G. Zhang, Q. Zhang, *Adv. Sci.* **2016**, *3*, 1500213.
- [55] a) L. Borchardt, M. Oschatz, S. Paasch, S. Kaskel, E. Brunner, *Phys. Chem. Chem. Phys.* **2013**, *15*, 15177–15184; b) Y. Gogotsi, A. Nikitin, H. Ye, W. Zhou, J. E. Fischer, B. Yi, H. C. Foley, M. W. Barsoum, *Nat. Mater.* **2003**, *2*, 591–594.
- [56] S. Thieme, J. Brückner, I. Bauer, M. Oschatz, L. Borchardt, H. Althues, S. Kaskel, *J. Mater. Chem. A* **2013**, *1*, 9225.
- [57] B. Ravel, M. Newville, *J. Synchrotron Radiat.* **2005**, *12*, 537–541.

Manuscript received: August 20, 2020

Revised manuscript received: December 7, 2020

Version of record online: December 16, 2020